Quantification of intravoxel velocity standard deviation and turbulence intensity by generalizing phase-contrast MRI

Petter Dyverfeldt, Andreas Sigfridsson, John-Peder Escobar Kvitting and Tino Ebbers

Linköping University Post Print

Quantification of Intra-Voxel Velocity Standard Deviation and Turbulence Intensity by Generalizing Phase-Contrast MRI

Petter Dyverfeldt,[1] Andreas Sigfridsson,[1,2,3] John-Peder Escobar Kvitting,[2,4] Tino Ebbers[1,2]

[1] Division of Clinical Physiology, Department of Medicine and Care, Linköping University, Linköping, Sweden.

[2] Center for Medical Image Science and Visualization (CMIV), Linköping University, Linköping, Sweden.

[3] Division of Medical Informatics, Department of Biomedical Engineering, Linköping University, Linköping, Sweden.

[4] Division of Cardiothoracic Surgery, Department of Medicine and Care, Linköping University Hospital, Linköping, Sweden.

Correspondence: Petter Dyverfeldt, MSc, Division of Clinical Physiology,
                 Department of Medicine and Care, Linköping University,
                 SE-581 85 Linköping, Sweden. E-mail: petdy@imv.liu.se.

ABSTRACT

Turbulent flow, characterized by velocity fluctuations, is a contributing factor to the pathogenesis of several cardiovascular diseases. A clinical non-invasive tool for the assessment of turbulence is lacking, however. It is well known that the occurrence of multiple spin velocities within a voxel, during the influence of a magnetic gradient moment, causes signal loss in phase-contrast magnetic resonance imaging. In this paper, a mathematical derivation of an expression for the computation of the standard deviation of the blood flow velocity distribution within a voxel is presented. The standard deviation is obtained from the magnitude of phase-contrast magnetic resonance imaging signals acquired with different first gradient moments. By exploiting the relation between standard deviation and turbulence intensity, this method allows for quantitative studies of turbulence. For validation, the turbulence intensity in an in-vitro flow phantom was quantified and the results compared favorably with previously published laser Doppler anemometry results. This method has the potential to become an important tool for the non-invasive assessment of turbulence in the arterial tree.

Key words: Phase-contrast magnetic resonance imaging, Turbulent flow, Velocity distribution, Turbulence intensity.

INTRODUCTION

Blood flow in the normal arterial tree seems to be remarkably free of turbulence. Turbulent flow, however, has been implicated in the pathogenesis of several cardiovascular diseases (1), including the initiation and development of atherosclerosis (2-5). Although well-recognized risk factors for atherosclerotic arterial disease, such as smoking, hypertension, elevated levels of cholesterol and diabetes mellitus, have widespread systemic effects, atherosclerosis tends to develop at specific locations such as branch points, bifurcations and sharp bends. These predilection areas are characterized by disturbed hemodynamics and increased risk for turbulent flow. By correlating the hemodynamic disturbances with the site-specific inclination for developing atherosclerosis, one might be able to classify pro-atherosclerotic vascular flow. Turbulent flow has also been recognized at intracardiac and intraaortic sites in the vicinity of diseased heart valves and heart valve prostheses (1,6). Assessment of turbulence in those regions could potentially improve the design of valve-sparing procedures and of the prostheses themselves.

Within fluid dynamics, turbulence is often studied using Reynolds decomposition in which the velocity is separated into time-averaged velocity and time-varying fluctuating velocity. No clinical tool for the in-vivo assessment of turbulence is available. In principle, Doppler ultrasonic methods are able to measure regional velocity distributions non-invasively. Doppler-derived measures of turbulence intensity have been proposed based on computational simulations (7), in-vitro measurements (8), and in-vivo studies (9). Ultrasound can only study flow in single dimensions, however, and its application in the arterial tree is further limited by inadequate acoustic windows to many regions.

Turbulent flow has been studied using diffusion-weighted magnetic resonance imaging (MRI) sequences. In diffusion-weighted imaging, signal loss due to intra-voxel phase variations is used for computation of the molecular diffusivity. Kuhete (10) introduced the term turbulent diffusivity (or eddy diffusivity) and obtained a measure of turbulent diffusivity from a measurement of the signal attenuation observed in time-averaged images. Also based on diffusion theory, Gao and Gore (11) derived an expression describing how the spin echo signal amplitude in steady turbulent flow depends on different flow and imaging parameters. Using that expression, Gatenby and Gore (12) showed how the signal level downstream from a stenosis made of a plug with a central hole is affected by partial echo acquisitions of

varying degree. They fitted several partial echo acquisitions to a model for computation of the spatial distribution of turbulence distal to the stenosis. In-vivo application of this would appear to be difficult due to long scan time.

Using Fourier velocity encoding MRI (13,14), the velocity spectrum within a voxel can be sampled. This method is very time consuming and therefore of limited usefulness in-vivo. Development of dynamic imaging, such as k-t BLAST (Broad-use Linear Acquisition Speed-up Technique) to accelerate the acquisitions may enhance the applicability of Fourier velocity encoding (15).

Phase-contrast (PC) MRI is a powerful tool for quantification of cardiovascular blood flow (16,17). PC-MRI can measure flow in all directions at any position and provides great flexibility with respect to spatial and temporal resolution. Conventional PC-MRI, however, only measures a mean velocity, spatially averaged over the voxel and temporally averaged over the duration of the bipolar gradient. When multiple spin velocities are present within a voxel, a reduced PC-MRI signal magnitude can be expected. This is the case for turbulent flow, in which the velocity fluctuations gives rise to an intra-voxel spin velocity distribution that causes signal loss during the influence of a magnetic field gradient (18,19). In velocity measurements, this is an unwanted peculiarity and minimization of its effect has been frequently discussed (19-21). For other applications, signal loss can be seen as a source of information. Prince et al. (22), for example, have shown that the degree of PC-MRI signal loss can be correlated to the functional significance of a stenosis. That, in combination with the work of Oshinski and colleagues (19) who suggested that the turbulent fluctuation velocity is related to the signal loss, raises the possibility to obtain quantitative information from PC-MRI signal loss in turbulent flow. Pipe (23,24) has presented a method for estimating the standard deviation (SD) of the velocity distribution within a voxel from a PC-MRI data acquisition. The presented theory was partly based on an empirically derived expression. Some in-vivo results depicting the velocity SD were included but quantitative results were not presented.

In this work, we mathematically derive a general expression for the computation of the SD of the blood flow velocity distribution within a voxel from a PC-MRI acquisition by assuming a certain spin velocity distribution. We validate this method by exploiting the close relation between SD and turbulence intensity and compare our findings on turbulence

intensity in in-vitro post-stenotic flow with previously reported results from laser Doppler anemometry measurements.

THEORY

In ordinary PC imaging, the velocities of moving spins are measured using bipolar velocity encoding gradients. A velocity encoding gradient has a first gradient moment of $M_1 = \int_0^T tG(t)\mathrm{d}t$ [T s^2 m^{-1}], where G is the gradient strength and T is the time of application. In a one-directional PC-MRI velocity acquisition, the velocity is extracted from the phase difference of two measurements with different first gradient moments. Such a measurement will be referred to here as a scan segment. The first gradient moments are related to the velocity encoding range (VENC) according to VENC = $\pi/(\gamma \Delta M_1)$ [m s^{-1}], where ΔM_1 is the net first gradient moment of the two scan segments and γ is the gyromagnetic ratio.

By studying the relation between PC-MRI signals acquired using different first gradient moments, the SD of the velocity can be derived. The derivation is based on the analytical expression for the signal of a voxel in presence of a first gradient moment

$$S(k_v) = C \int_{-\infty}^{\infty} s(v)e^{-ik_v v}\mathrm{d}v, \tag{1}$$

where C is a scaling factor influenced by relaxation parameters, spin density and receiver gain, v is the velocity, $s(v)$ is the spin velocity distribution within the voxel and $k_v = \gamma M_1$ [s m^{-1}]. By assuming that the spins within a voxel have a Gaussian velocity distribution, as done by Gao and Gore (11) and Gach and Lowe (25), $s(v)$ can be written as

$$s(v) = \frac{1}{\sigma\sqrt{2\pi}} e^{-\frac{1}{2\sigma^2}(v-v_m)^2}, \tag{2}$$

where σ denotes the SD and v_m is the mean velocity. Combining Eq. 1 and Eq. 2 gives the following expression for the PC-MRI signal:

$$S(k_v) = Ce^{-\frac{\sigma^2 k_v^2}{2} - iv_m k_v}. \tag{3}$$

By combining the expressions of two scan segments with different first gradient moment so that $|k_{v_1}| \neq |k_{v_2}|$, the scaling factor C can be eliminated since the receiver gain, relaxation

effects and spin density are not affected by the first gradient moment. The signals of two such scan segments are related to each other according to

$$S(k_{v_1}) = S(k_{v_2})e^{-\frac{\sigma^2(k_{v_1}^2 - k_{v_2}^2)}{2} - iv_m(k_{v_1} - k_{v_2})}. \qquad [4]$$

In PC velocity imaging, the imaginary part of the exponent in Eq. 4 is the part of interest. Since σ, however, is located in the real part of the exponent, we are only interested in the magnitude of the expression. Taking the absolute value of Eq. 4 results in an expression that describes how the magnitude of two PC-MRI signals are related to the SD,

$$\left|S(k_{v_1})\right| = \left|S(k_{v_2})\right|e^{-\frac{\sigma^2(k_{v_1}^2 - k_{v_2}^2)}{2}}. \qquad [5]$$

By rearranging Eq. 5, an expression for the SD is obtained,

$$\sigma = \sqrt{\frac{2\ln\left(\frac{\left|S(k_{v_2})\right|}{\left|S(k_{v_1})\right|}\right)}{k_{v_1}^2 - k_{v_2}^2}} \ [\text{m s}^{-1}]. \qquad [6]$$

This expression states that the SD of the velocity distribution within a voxel, in one direction, can be computed from two PC-MRI scan segments of different first gradient moments. For the case of $k_{v_2} = 0$ this is equivalent to the empirical expression derived by Pipe. Our method is valid for all values of k_v (with the restriction that $|k_{v_1}| \neq |k_{v_2}|$) and can thus be considered as more general. In order to maximize the accuracy in presence of noise, however, one of the scan segments should be carried out using zero first gradient moment ($k_v = 0$). The signal of such a scan segment will be referred to as the reference signal $S(0)$. The first gradient moment in the other scan segment should be adapted to the expected SD. For simultaneous acquisition of the SD in three directions, three scan segments velocity encoded in mutually perpendicular directions and one scan segment with zero first gradient moment are preferred. This is exactly the outcome of an acquisition velocity encoded by the non-symmetric simple four-point method (26). While normally the velocity is extracted from the phase difference of $S(0)$ and $S(k_v)$, Eq. 6 makes it possible to obtain the SD of the velocity distribution within a voxel from the magnitude of $S(0)$ and $S(k_v)$. By considering turbulent velocity fluctuations within a voxel

to be an ergodic process, in which ensemble averages can be exchanged for time averages, the turbulence intensity can be obtained by dividing the SD of the velocity with the cross-sectional mean velocity (19,27,28). This quantity allows for comparative studies of the level of turbulence in different flow situations.

The fact that Eq. 1 is a Fourier transform creates another way to explain the theory. $S(k_v)$ and $s(v)$ both describes the spin velocity distribution and constitute a Fourier transform pair. Since we assume that the spin velocity distribution is Gaussian with an SD of σ, $|S(k_v)|$ is also Gaussian with an SD related to σ as illustrated in
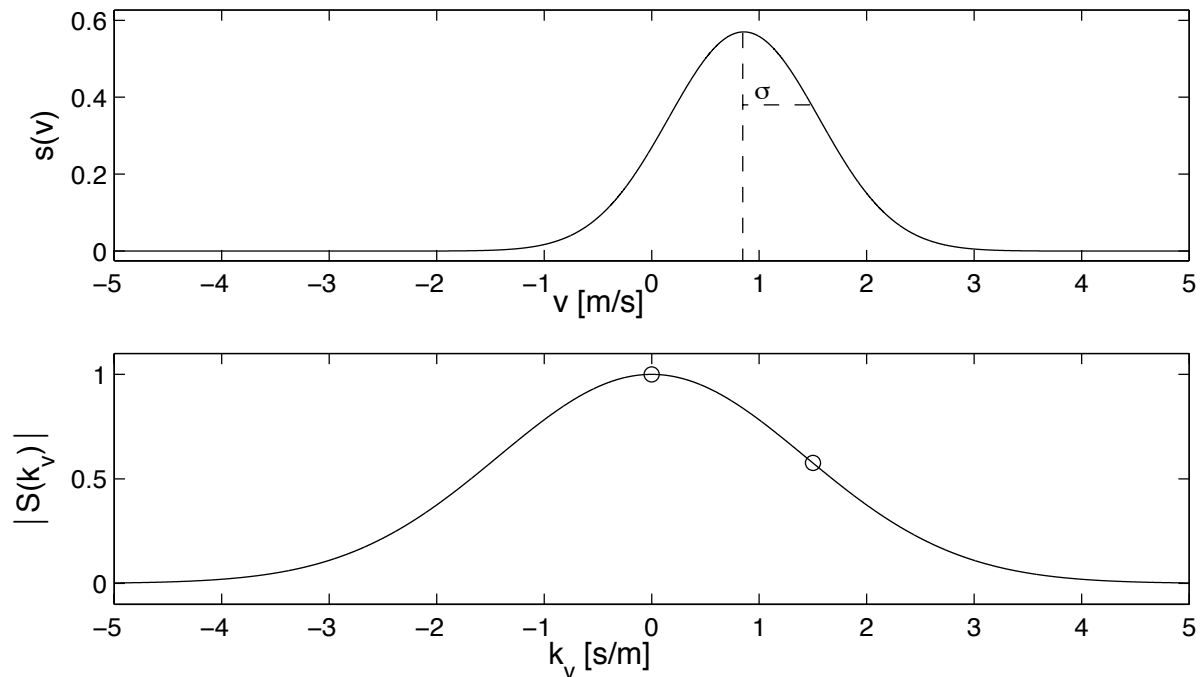
Fig. **1**. In order to derive σ, two points on $|S(k_v)|$ are measured. A Gaussian function is fitted to these points, after which the Fourier transform relationship is exploited in order to compute σ. This can be compared with Fourier velocity encoding, where k_v in Eq. 1 is varied in a stepwise manner to obtain the Fourier transform of the velocity distribution for an image voxel. With our assumption of a Gaussian spin velocity distribution, the complete spectrum can be obtained from only two measurements. The theory can readily be adapted to other, non-Gaussian, distributions, which have a Fourier transform that is invertible on a range of k_v-values greater than zero. A Lorentzian or a boxcar spin velocity distribution, for example, could be treated in the same manner although with other measures of statistical dispersion than the SD (table 1).

METHODS

Measurement setup

We constructed an in-vitro flow phantom consisting of a Perspex tube with a 75 % area reduction, cosine-shaped stenosis and compared our results on turbulence intensity with published laser Doppler anemometry results (27). Denoting the radius of the un-occluded part of the phantom as a and letting r and z be the radial and axial distance from the center of the stenosis, which, when divided by a, form the dimensionless variables R and Z, the contour of the phantom is described by

$$R = r/a = \begin{cases} 1-(1+\cos(Z\pi/2))/4, & -2 < Z < 2 \\ 1, & |Z| > 2 \end{cases} \qquad [7]$$

The phantom used in the published laser Doppler anemometry study had a diameter of 50.4 mm and a length of more than 6 meters. In order to fit the phantom into the MRI scanner, the phantom needed to be downsized. By regarding all the measures of length of the phantom as dimensionless properties proportional to the un-occluded tube diameter, a uniform downscaling of the phantom was achieved that maintained the shape of the stenosis. This resulted in a flow phantom, comparable to a human-sized vessel stenosis, with an un-occluded tube diameter of 14.6 mm (
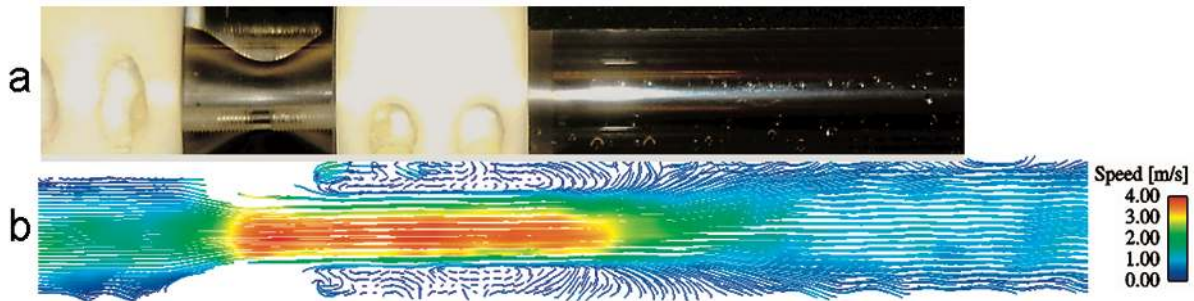

Fig. 2a). The entrance length of the phantom was 1.5 meters, ensuring fully developed flow, and the length distal to the stenosis was 0.5 meters. The fluid used in the experiments was a blood-mimicking 63 % glycerol and 37 % water solution maintained at a temperature of 33 °C, giving it a kinematic viscosity of 0.12 cm^2/s. A computer controlled displacement pump (CardioFlow 1000 MR, Shelley Medical Imaging Technologies, London, ON, Canada) generated the flow.

Flow settings corresponding to three different Reynolds numbers (Re) were used in the comparison. The Reynolds number is defined as $Re = v_cD/\upsilon$ [-] (29), where v_c is the mean cross-sectional velocity, D is the un-occluded tube diameter and υ is the kinematic viscosity. As turbulence intensity is dimensionless, no scaling was necessary for comparison.

Data acquisitions

PC measurements with four interleaved velocity encoded scan segments were carried out to acquire three-dimensional three-directional SD, and velocity, data using a clinical 1.5 T MRI scanner (Philips Achieva, Philips Medical Systems, Best, The Netherlands). The pulse sequences were optimized for measuring the highest expected SD at each flow setting. One of the scan segments had zero first gradient moment and the other three had a first gradient moment such that VENC was somewhat larger than the expected SD. The frequency encoding direction was perpendicular to the flow in order to avoid displacement artifacts (30). Measurements were performed at three flow settings (table 2) characterized by different Re upstream to the stenosis of 500, 1000 and 2000 respectively. This corresponds to Re of 1000, 2000 and 4000 at the center of the stenosis, which ensures turbulent flow for the two last flow settings (27). The repetition time (15 ms) and the flip angle (20 °) were kept constant and the echo time was the shortest possible (table 2). The field of view was 130 x 97.5 x 160 mm with a matrix size of 64 x 48 x 80 (2 x 2 x 2 mm voxel size) and the total scan time was 5 min 27 sec.

In addition to these measurements, the following complementary measurements were carried out at Re 1000 using the same spatial resolution: A velocity measurement (VENC = 400 cm/s, TE = 3.1 ms), two SD measurements with different first gradient moment (VENC = 90 cm/s, TE = 3.5 ms and VENC = 60 cm/s, TE = 3.8 ms) and an SD measurement with a sensitivity encoding (SENSE) reduction factor of two (VENC = 60 cm/s , TE = 3.8 ms).

Post-processing

After image reconstruction, computations were carried out in MATLAB (The MathWorks Inc, Natick, MA, USA). The SD was computed by means of Eq. 6. The mean flow velocity for converting into turbulence intensity was taken from the calibrated pump settings.

Equation 6 implies that if the expression under the square root sign is less than zero (with our choice of parameters, $|S(k_v)| > |S(0)|$), the estimate of SD becomes undefined. Theoretically, $S(0)$ should have less phase dispersion and thereby greater magnitude than $S(k_v)$ but due to noise $|S(0)|$ may become smaller than $|S(k_v)|$ in areas with low flow disorder. In the computations of SD, such areas have been regarded as containing undisturbed flow with zero SD.

The velocity measurement at Re 1000 was transferred into Ensight$^{©}$ (CEI Inc, Research Triangle Park, NC, USA) for streamline visualization (31).

In computations concerning the centerline magnitude and thus the SD and the turbulence intensity, bilinear interpolation of the closest in-plane pixels has been used for extracting the magnitude value in the center point of the tube in each slice.

RESULTS

In the result plots, the non-dimensional measures of length Z and Y, normalized by the un-occluded tube diameter (14.6 mm for our phantom and 50.4 mm for the laser Doppler anemometry phantom), are used to facilitate the comparison. $|S(0)|$ represents the magnitude of a signal acquired with zero first gradient moment and $|S(k_v)|$ represents the magnitude of a velocity encoded signal acquired with a first gradient moment adapted to the expected maximum SD. Velocity encoding was applied in the X-, Y- and Z-directions. The Z-direction is the direction of flow whereas the X- and Y-directions are perpendicular to the flow.

Some characteristics of post-stenotic flow appear in the visualization of the velocity measurement at Re 1000. The streamlines in
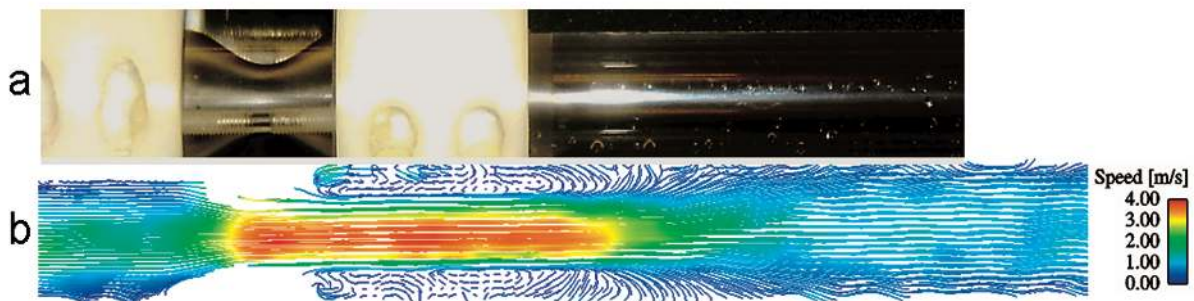

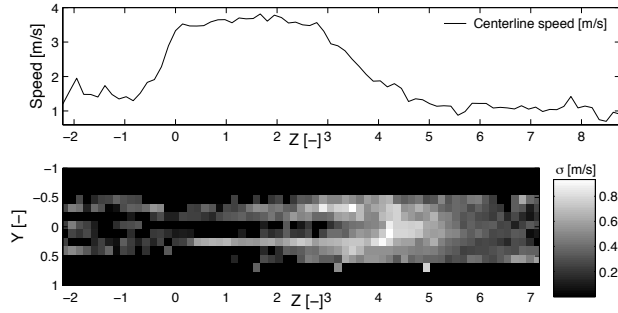Fig. **2**b show a recirculation zone surrounding a flow jet distal to the stenosis and the speed plot in

Fig. 3 (upper panel) shows a plateau of high centerline speed at Z > 0 that suddenly decreases at Z ≈ 3. The SD map in
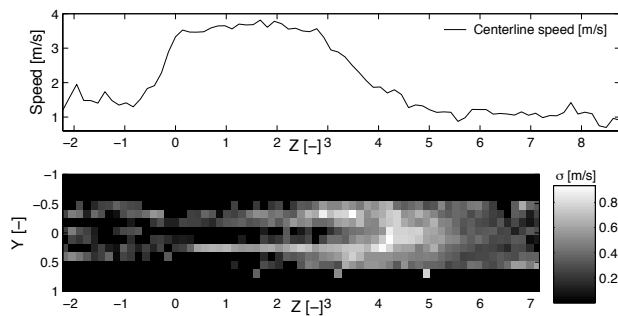

Fig. 3 (lower panel), computed from the reconstructed magnitude data of the SD measurement at Re 1000, depicts low SD in the center of the flow jet and high SD distal to the point where the speed decreases. A comparison of the SD maps for the three flow settings described in table 2 can be seen in Fig. 4.

The results of the SD measurements at Re 1000 with a VENC of 120 cm/s are presented in Figs. 5-7. Figure 5 shows the reconstructed magnitude values along the centerline of the phantom for all scan segments. These magnitude values were used for computing the SD
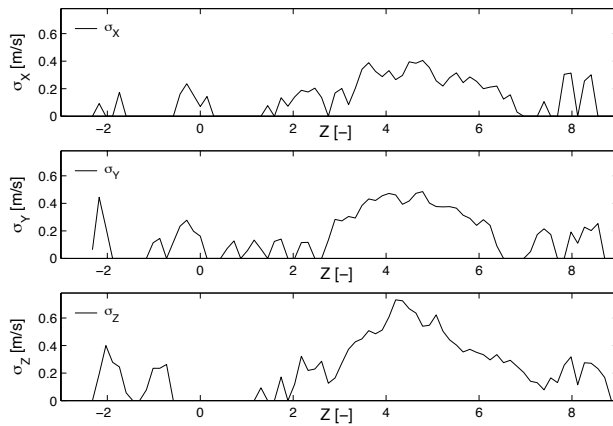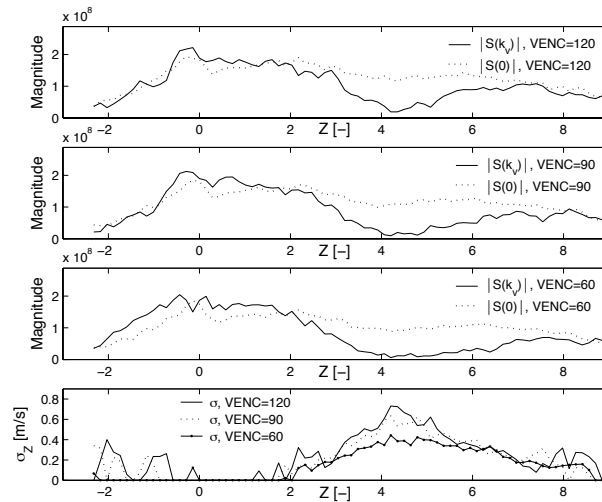
shown in

Fig. 6 and consequently, in combination with the mean flow velocity, the turbulence
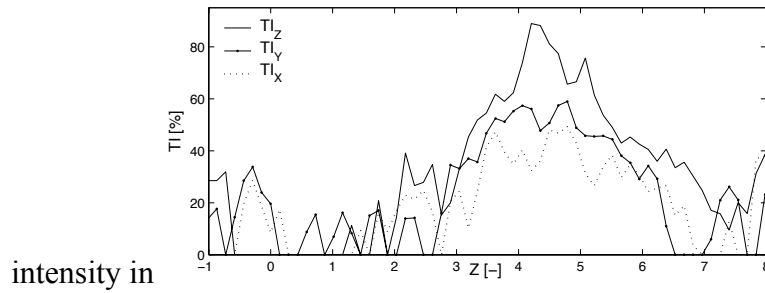
intensity in

Fig. 7. It is notable that noise distinctively affects the SD and turbulence intensity in the areas where $|S(0)|$ and $|S(k_v)|$ in principle overlap, as in $-2 < Z < 2$.

The effect of using different first gradient moments in SD measurements at identical

flow settings (Re 1000) is presented in

Fig. **8**. Different first gradient moments were obtained using three different VENC's (60, 90 and 120 cm/s). Note that $|S(k_v)|$ for VENC 60 is close to zero at $3.5 < Z < 6$ and that the maximum SD for this acquisition is lower than for the other acquisitions.

The centerline magnitude and SD from the measurement with and without SENSE, where VENC is 60 cm/s in both cases, can be seen in
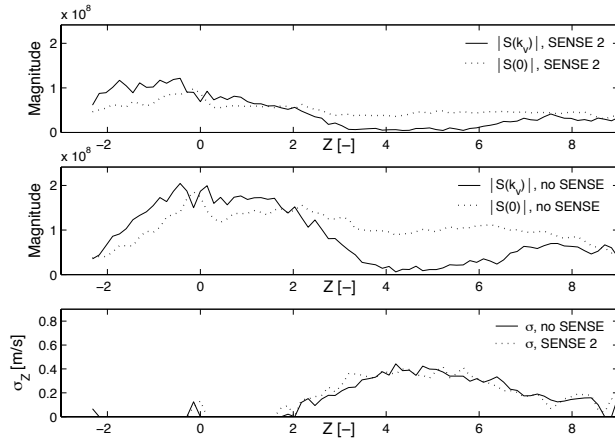
Fig. 9. We observe that the SD has the same appearance with and without SENSE. The comparison with the laser Doppler anemometry results can be seen in
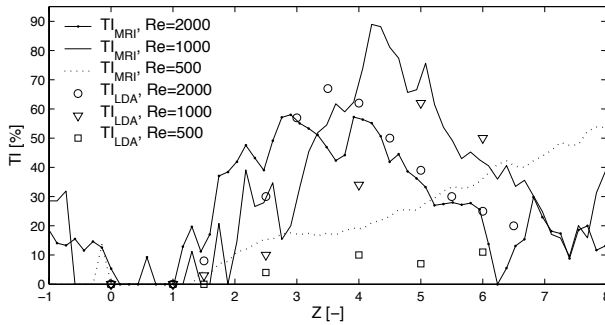

Fig. 10. The turbulence intensity obtained from MRI measurements has the same outline as the laser Doppler anemometry results. Further, the location and degree of peak turbulence intensity between different Reynolds numbers show reasonable agreement with the laser Doppler anemometry results as well.

DISCUSSION

We have validated a method for direct measurement of the SD of the blood flow velocity distribution within a voxel by comparing results of turbulence intensity from an in-vitro post-stenotic flow phantom with previously reported experimental results using laser Doppler anemometry. The results agree with the derived theory, which emphasizes the potential of the method presented here for measuring SD and quantifying turbulence intensity.

According to the theory presented here, pulse sequence parameters other than the first gradient moments that are known to affect the signal magnitude, such as echo time and gradient timing (20), should only affect the accuracy of the measured SD and not its value. In

addition, use of SENSE should not affect the SD value, which agrees with our in-vitro findings.

The proposed method has some obvious similarities with diffusion-weighted imaging. Equation 5 can be compared to the diffusion-weighted imaging expression $S/S_0 = e^{-bD}$ where D is known as the diffusion constant and b is a factor depending on the magnetic field gradients and their timing (32). This expression reflects the diffusion as the relative signal loss of two diffusion-weighted MRI measurements whereas Eq. 5 reflects the SD of the velocity distribution within a voxel as the relative signal loss of two PC-MRI scan segments. In spite of these similarities, due to the relatively low first gradient moment, the diffusion effects are negligible in an SD measurement.

In absence of noise, any values of k_v (except $|k_{v1}| = |k_{v2}|$) can be used to compute the SD within a voxel using Eq. 6. In practice, however, the presence of noise requires that one of the first gradient moments, k_{v1} or k_{v2}, used in an SD acquisition is adapted to the expected SD. Guidelines on the choice of k_{v1} and k_{v2} can be provided. One scan segment is preferably carried out with $k_v = 0$ in order to obtain maximal signal magnitude. k_v for the other scan segment should be chosen in such manner that the best precision is obtained in the fit of the Gaussian $|S(k_v)|$-function. This is achieved with a k_v positioned in the regime of $|k_v| = 1/\sigma$ where $|S(k_v)|$ has its steepest gradient. Since we are studying the magnitude of the complex MR signal, $|S(k_v)|$ is, due to noise, likely to be overestimated at small values of $|S(k_v)|$. Consequently, at excessively large values of k_v, noise will limit the maximum SD that can be resolved. Figure 8 shows the effect of choosing a k_v that is too large to resolve the maximum SD at the level of noise present. In the laser Doppler anemometry comparison (
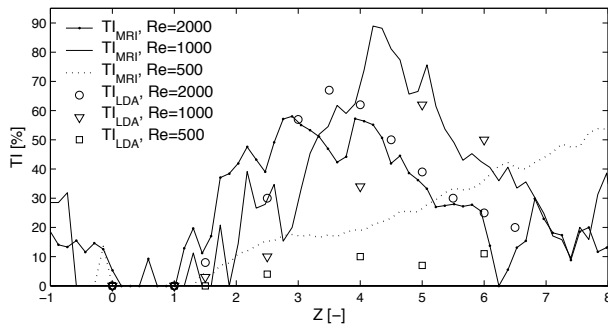

Fig. 10), the flat top of the turbulence intensity curve at Re 2000 measured with our method is also a result of a k_v that was unable to resolve the largest SD's due to noise. If k_v is

too small it will be hard to obtain an accurate fit of the Gaussian $|S(k_v)|$-function. In areas of low SD, the Gaussian $|S(k_v)|$-function decays more slowly than for high SD, implying that a larger value of k_v is needed to obtain an accurate fit of the $|S(k_v)|$-function. A k_v suitable for measuring high SD thus provides low accuracy at low SD as seen in the pre-stenotic region in
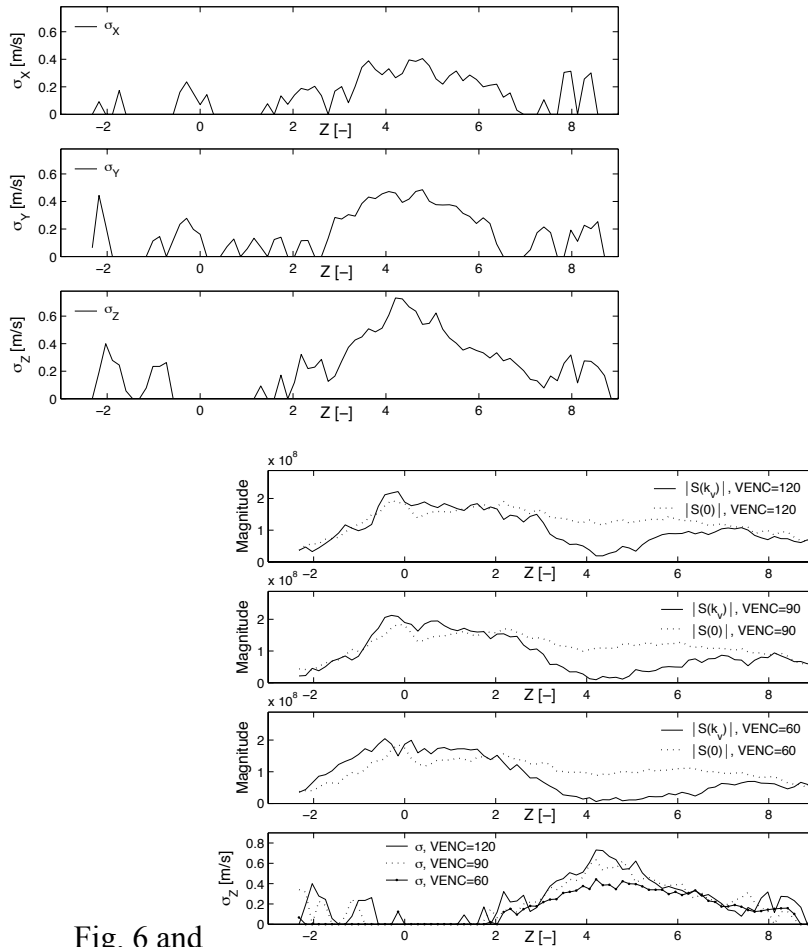

Fig. 6 and

Fig. **8**.

From the theory as well as the measurements, it can be concluded that the effect of noise is substantial. Maximization of the signal-to-noise ratio is thus an issue that needs to be considered. Post-processing techniques can lead to considerable improvements, but the best effect on the signal-to-noise ratio is expected from improvements in the acquisitions. Acquiring data post contrast agent injection, increasing the number of signal averages or increasing the voxel size are the most obvious options. An increased number of signal averages will result in an increased scan time, which is undesirable for in-vivo three-dimensional measurements. Two-dimensional acquisitions may therefore be more convenient for in-vivo studies. In two-dimensional Fourier velocity encoding, the saturation effects of

spins with different velocities have to be considered in measurements of the spin velocity distribution (33). A related problem appears in two-dimensional SD imaging where the saturation effects will influence the scaling factor C (Eq. 1). In three-dimensional imaging, steady state is usually obtained inside the imaging volume and these effects can easily be avoided. An increased voxel size as well as use of non-isotropic voxels may affect the results and their influence needs further investigation.

The theory requires that the spin velocities can be assumed to have a certain distribution and the derived expression for computing the SD (Eq. 6) is valid under the condition that the spin velocity distribution is Gaussian. Partial volume will result in a complicated appearance of $|S(k_v)|$ and the spin velocity distribution will contain more unknown parameters than what can be computed from two measurements of $S(k_v)$. Voxels with velocity partial volume effects will also cause complications in SD measurements. In-vivo, where cardiac gating techniques will be necessary, acceleration may affect the SD measurements. Solely temporal acceleration is not expected to affect the measured SD. Spatial acceleration, on the other hand, will contribute to the measured SD. In cardiovascular blood flow, however, the range of intra-voxel spin velocities resulting from spatial acceleration is most often small compared to the range of velocities resulting from turbulent velocity fluctuations. In this case, spatial acceleration should have a minor effect on the measured SD. Close to the vessel walls, where the highest spatial acceleration is expected, the effect may be more notable. Before SD and turbulence intensity can be assessed near the vessel wall, further investigation is needed on acceleration and partial volume effects.

Since the same pulse sequence can be used for an SD measurement and a PC-MRI velocity measurement, it is theoretically possible to measure velocity and SD simultaneously. In order to avoid velocity aliasing, however, a velocity measurement usually requires a smaller k_v (higher VENC) than what is optimal for an SD measurement. By increasing the signal-to-noise ratio, it could be possible to obtain both a sufficiently accurate SD and, after phase unwrapping, the velocity out of the same data set.

Concepts from other MR imaging techniques could also be applicable in SD imaging. Tensors, used in diffusion tensor imaging, for example, could be used to describe the SD and turbulence intensity in all spatial directions in areas of anisotropic turbulence.

The proposed method may be useful in several applications where a non-invasive tool to study turbulent flow is needed. The SD maps in Fig. 4 hint that the method has excellent capacity for visualization of turbulent flow. Visualization of SD and turbulence intensity maps would provide a new aspect in the assessment of cardiovascular function, for example in the evaluation of valve-sparing surgery and the design of heart valve prostheses. Understanding how design parameters influence turbulence and its impact on prosthetic performance and cardiac efficiency of the prostheses could lead to new approaches in these fields. With respect to vascular function, the efficiency of fluid transport increases with higher laminar flow rates, implying that in many cases optimal blood flow velocity is close to turbulent flow thresholds. Even a small disturbance of the flow can thus give rise to turbulence. Hemodynamic forces regulate endothelial cell function, and turbulent flow has been correlated with endothelial processes leading to atherosclerosis (2). By localizing and analyzing areas of turbulent flow at an early stage, these areas of risk for developing atherosclerotic plaque can be identified. Non-invasive correlation of turbulence intensity with endothelial responses such as surface receptor and gene alterations would open new avenues for disease recognition and management.

CONCLUSION

We have mathematically derived a general expression for the computation of the SD of the velocity distribution within a voxel from a PC-MRI acquisition. This method allows for quantitative analysis of turbulent flow and enables combined studies of flow velocity and turbulence intensity. An underlying theory has been outlined and our results on turbulence intensity correlate well with previous laser Doppler anemometry data. This approach to the measurement of SD and quantification of turbulence intensity may allow non-invasive assessment of turbulence in the normal and atherosclerotic arterial tree.

ACKNOWLEDGEMENTS

REFERENCES
1.	Nichols WW, O'Rourke MF. The nature of flow of a liquid. McDonald's Blood Flow in Arteries. 5 ed. London: Hodder Arnold; 2005.
2.	Brooks AR, Lelkes PI, Rubanyi GM. Gene expression profiling of vascular endothelial cells exposed to fluid mechanical forces: relevance for focal susceptibility to atherosclerosis. Endothelium 2004;11(1):45-57.
3.	Galley HF, Webster NR. Physiology of the endothelium. Br J Anaesth 2004;93(1):105-113.
4.	Malek AM, Alper SL, Izumo S. Hemodynamic shear stress and its role in atherosclerosis. Jama 1999;282(21):2035-2042.
5.	VanderLaan PA, Reardon CA, Getz GS. Site specificity of atherosclerosis: site-selective responses to atherosclerotic modulators. Arterioscler Thromb Vasc Biol 2004;24(1):12-22.
6.	Stein PD, Sabbah HN. Turbulent blood flow in the ascending aorta of humans with normal and diseased aortic valves. Circulation research 1976;39(1):58-65.
7.	Cloutier G, Chen D, Durand LG. Performance of time-frequency representation techniques to measure blood flow turbulence with pulsed-wave Doppler ultrasound. Ultrasound Med Biol 2001;27(4):535-550.
8.	Poepping TL, Nikolov HN, Rankin RN, Lee M, Holdsworth DW. An in vitro system for Doppler ultrasound flow studies in the stenosed carotid artery bifurcation. Ultrasound Med Biol 2002;28(4):495-506.
9.	Isaaz K, Bruntz JF, Da Costa A, Winninger D, Cerisier A, de Chillou C, Sadoul N, Lamaud M, Ethevenot G, Aliot E. Noninvasive quantitation of blood flow turbulence in patients with aortic valve disease using online digital computer analysis of Doppler velocity data. J Am Soc Echocardiogr 2003;16(9):965-974.
10.	Kuethe DO. Measuring distributions of diffusivity in turbulent fluids with magnetic-resonance imaging. Physical Review A 1989;40(8):4542-4551.
11.	Gao JH, Gore JO. Turbulent flow effects on NMR imaging: measurement of turbulent intensity. Med Phys 1991;18(5):1045-1051.
12.	Gatenby JC, Gore JC. Mapping of turbulent intensity by magnetic resonance imaging. J Magn Reson B 1994;104(2):119-126.
13.	Moran PR. A flow velocity zeugmatographic interlace for NMR imaging in humans. Magn Reson Imaging 1982;1(4):197-203.
14.	Redpath TW, Norris DG, Jones RA, Hutchison JM. A new method of NMR flow imaging. Phys Med Biol 1984;29(7):891-895.
15.	Hansen MS, Baltes C, Tsao J, Kozerke S, Pruessmann KP, Boesiger P, Pedersen EM. Accelerated dynamic Fourier velocity encoding by exploiting velocity-spatio-temporal correlations. Magma 2004;17(2):86-94.
16.	Pelc NJ, Herfkens RJ, Shimakawa A, Enzmann DR. Phase contrast cine magnetic resonance imaging. Magn Reson Q 1991;7(4):229-254.
17.	Lotz J, Meier C, Leppert A, Galanski M. Cardiovascular flow measurement with phase-contrast MR imaging: basic facts and implementation. Radiographics 2002;22(3):651-671.
18.	Hamilton CA, Moran PR, Santago P, 2nd, Rajala SA. Effects of intravoxel velocity distributions on the accuracy of the phase-mapping method in phase-contrast MR angiography. J Magn Reson Imaging 1994;4(5):752-755.

19. Oshinski JN, Ku DN, Pettigrew RI. Turbulent fluctuation velocity: the most significant determinant of signal loss in stenotic vessels. Magn Reson Med 1995;33(2):193-199.
20. Stahlberg F, Thomsen C, Sondergaard L, Henriksen O. Pulse sequence design for MR velocity mapping of complex flow: notes on the necessity of low echo times. Magn Reson Imaging 1994;12(8):1255-1262.
21. Siegel JM, Jr., Oshinski JN, Pettigrew RI, Ku DN. The accuracy of magnetic resonance phase velocity measurements in stenotic flow. J Biomech 1996;29(12):1665-1672.
22. Prince MR, Schoenberg SO, Ward JS, Londy FJ, Wakefield TW, Stanley JC. Hemodynamically significant atherosclerotic renal artery stenosis: MR angiographic features. Radiology 1997;205(1):128-136.
23. Pipe JG. A simple measure of flow shear and turbulence. Proc Intl Mag Reson Med 9 2001:1971.
24. Pipe JG. A simple measure of flow disorder and wall shear stress in phase contrast MRI. Magn Reson Med 2003;49(3):543-550.
25. Gach HM, Lowe IJ. Measuring flow reattachment lengths downstream of a stenosis using MRI. J Magn Reson Imaging 2000;12(6):939-948.
26. Pelc NJ, Bernstein MA, Shimakawa A, Glover GH. Encoding strategies for three-direction phase-contrast MR imaging of flow. J Magn Reson Imaging 1991;1(4):405-413.
27. Ahmed SA, Giddens DP. Flow disturbance measurements through a constricted tube at moderate Reynolds numbers. J Biomech 1983;16(12):955-963.
28. Deshpande MD, Giddens DP. Turbulence measurements in a constricted tube. J Fluid Mech 1980;97(1):65-89.
29. White FM. Viscous Flow in Ducts. Fluid Mechanics. 3 ed. Hightstown: McGraw-Hill Inc.; 1994.
30. Thunberg P, Wigström L, Ebbers T, Karlsson M. Correction for displacement artifacts in 3D phase contrast imaging. J Magn Reson Imaging 2002;16(5):591-597.
31. Wigström L, Ebbers T, Fyrenius A, Karlsson M, Engvall J, Wranne B, Bolger AF. Particle trace visualization of intracardiac flow using time-resolved 3D phase contrast MRI. Magn Reson Med 1999;41(4):793-799.
32. Stejskal EO, Tanner JE. Spin diffusion measurements: spin echoes in the presence in a time-dependent field gradient. J Chem Phys 1965;42(1):288-292.
33. Tsai CM, Olcott EW, Nishimura DG. Flow quantification using low-spatial-resolution and low-velocity-resolution velocity images. Magn Reson Med 1999;42(4):682-690.
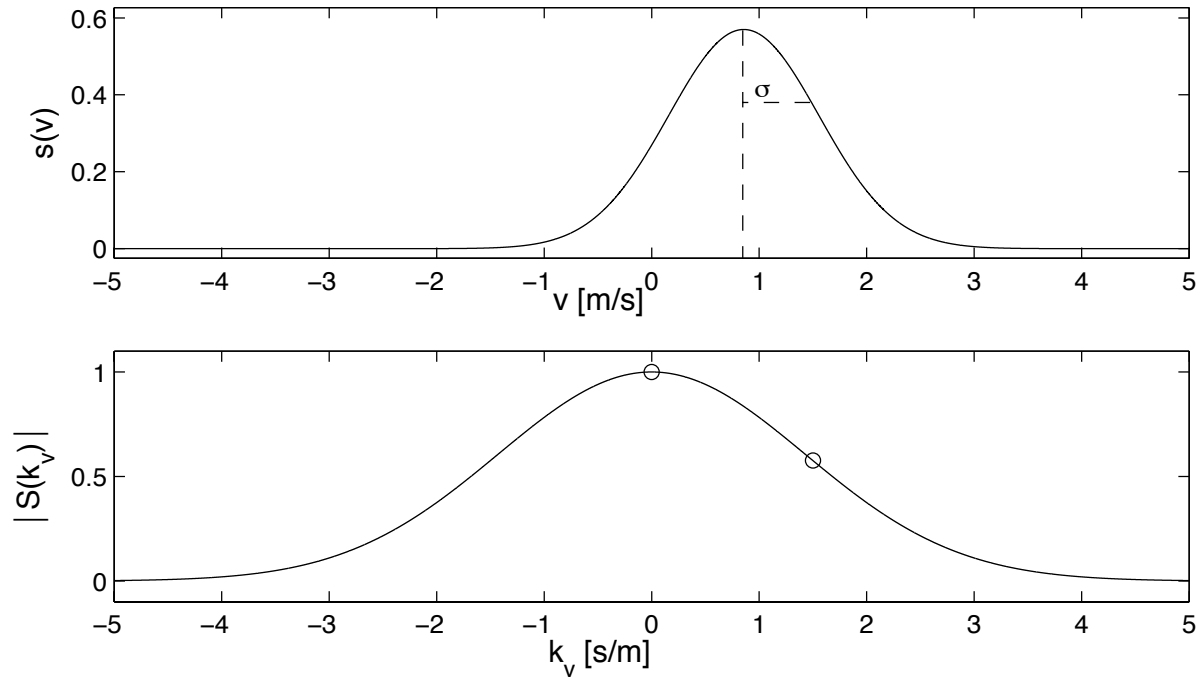
Fig. 1. A schematic of the relationship between a Gaussian spin velocity distribution *s(v)* (upper panel) and the absolute value of its Fourier transform, *|S(k$_v$)|* (lower panel). The SD, σ, of the spin velocity distribution is derived by exploiting the Fourier transform relationship with *|S(k$_v$)|*. Two measurements of *|S(k$_v$)|*, as indicated by the circles, are used to compute σ.
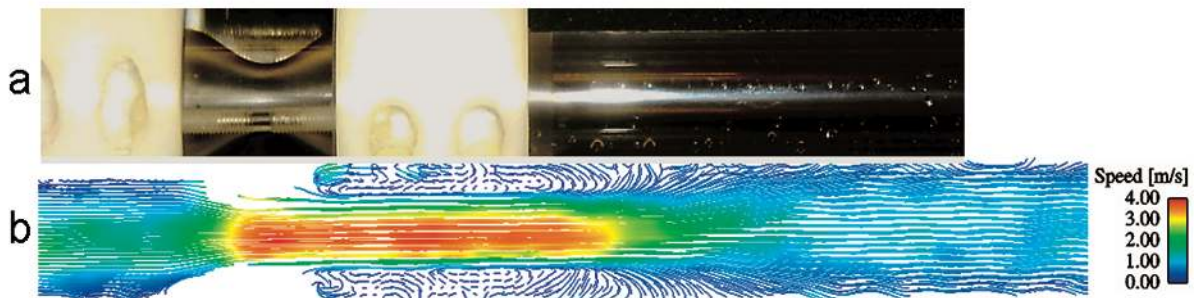

Fig. 2. a) A picture of the in-vitro flow phantom. Plexiglas tubes are attached to both ends of the Plexiglas cosine shaped stenosis. The joints are sealed by o-ring gaskets and Delrin clips (the white parts in the picture) are used to fasten the joints. b) A streamline visualization of the flow at Re 1000.
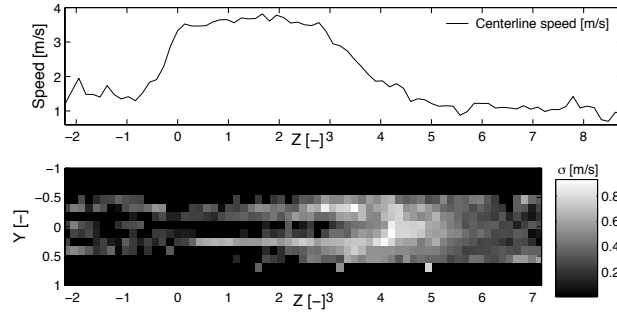
Fig. 3. Speed and SD at Re 1000. The upper panel shows a plot of the speed along the centerline of the phantom at Re 1000. The lower panel shows an SD map at Re 1000, velocity encoded in the Z-direction. Z and Y show the normalized distance from the center of the stenosis (Z, Y = 1 ⇔ 14.6 mm) as described by Eq. 7. The direction of flow is the positive Z-direction.
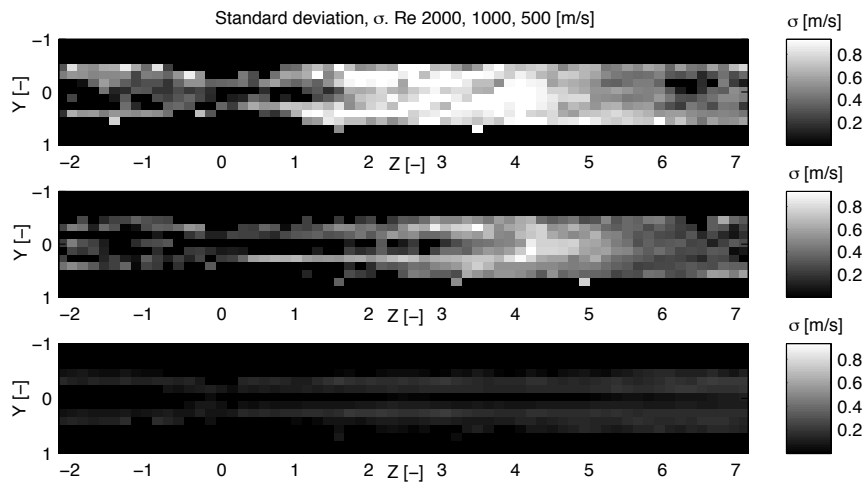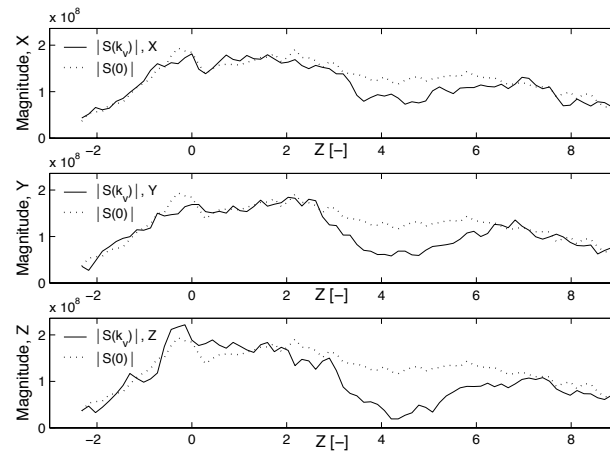

Fig. 4. SD maps for Re 2000 (upper panel), 1000 (middle panel) and 500 (lower panel), velocity encoded in the Z-direction. Z and Y show the normalized distance from the center of the stenosis (Z, Y = 1 ⇔ 14.6 mm) as described by Eq. 7. The direction of flow is the positive Z-direction.

Fig. 5. Centerline signal magnitude in the X-, Y- and Z-direction at Re 1000. $|S(0)|$ (dotted line) is the magnitude of the reference signal and $|S(k_v)|$ (solid line) is the signal velocity encoded in the given direction. Z shows the normalized distance from the center of the stenosis (Z = 1 ⇔ 14.6 mm) as described by Eq. 7. The direction of

flow is the positive Z-direction. These (measured) magnitude values were used for computing the SD that
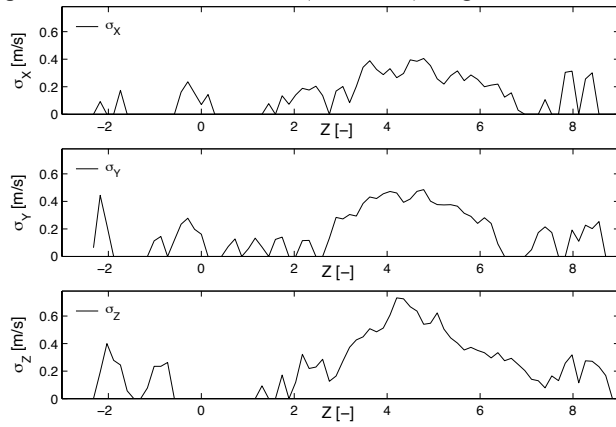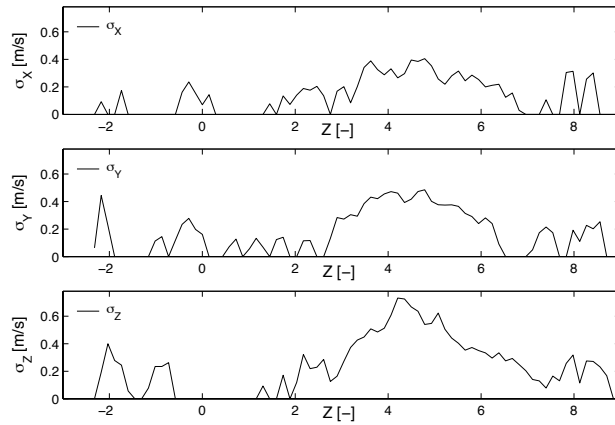

appears in

Fig. 6.

Fig. 6. Centerline SD, σ, in the X-, Y- and Z-direction at Re 1000. Z shows the normalized distance from the center of the stenosis ($Z = 1 \Leftrightarrow 14.6$ mm) as described by Eq. 7. The direction of flow is the positive Z-direction. These SD values were used for computing the turbulence intensity that appears in
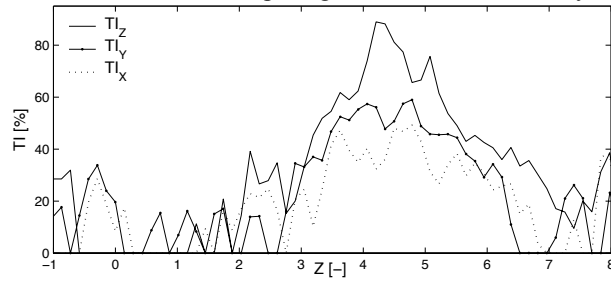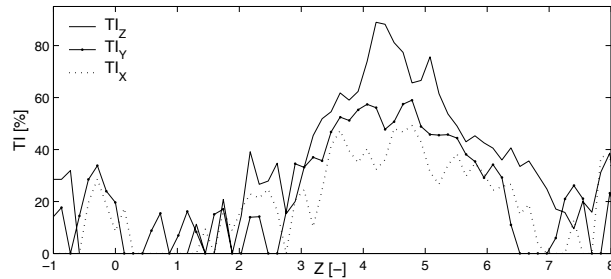

Fig. 7.

Fig. 7. Centerline turbulence intensity (TI) at Re 1000 in the X- (solid line), Y- (dashed line) and Z-direction (dotted line). Z shows the normalized distance from the center of the stenosis (Z = 1 ⇔ 14.6 mm) as described by Eq. 7. The direction of flow is the positive Z-direction.
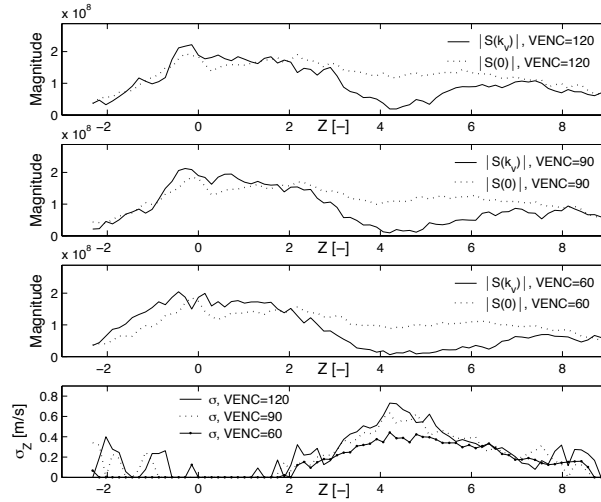

Fig. 8. VENC comparison. Centerline signal magnitude and centerline SD at Re 1000 in the Z-direction acquired using three different VENC's. Z shows the normalized distance from the center of the stenosis (Z = 1 ⇔ 14.6 mm) as described by Eq. 7. The direction of flow is the positive Z-direction.
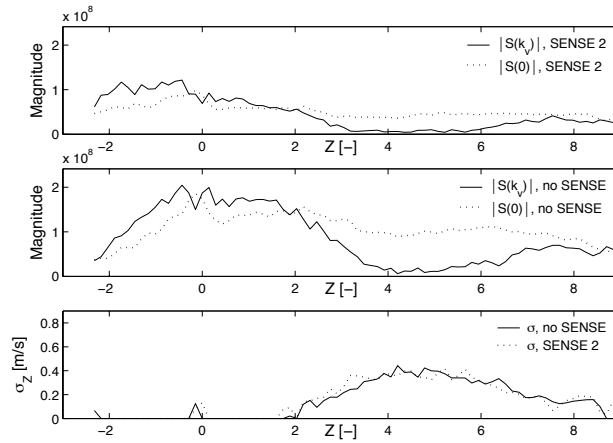

Fig. 9. SENSE comparison. Centerline signal magnitude and centerline SD at Re 1000 with VENC = 60 cm/s in the Z-direction acquired with and without SENSE. Z shows the normalized distance from the center of the stenosis (Z = 1 ⇔ 14.6 mm) as described by Eq. 7. The direction of flow is the positive Z-direction.
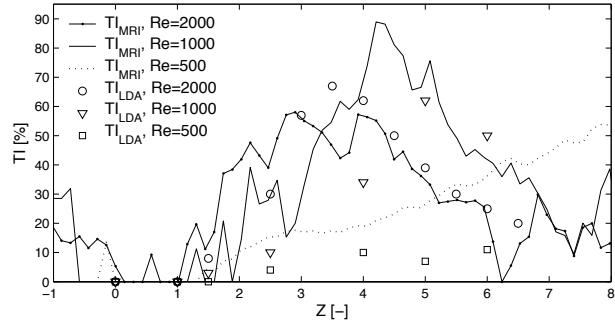
Fig. 10. Laser Doppler anemometry (LDA) comparison. Centerline turbulence intensity (TI) for Re 500, 1000, 2000 (the three flow settings in table 2) in the Z-direction as measured with MRI and LDA. Z shows the normalized distance from the center of the stenosis as described by Eq. 7. The direction of flow is the positive Z-direction. The use of the non-dimensional measure of length Z facilitates the comparison. Z = 1 corresponds to 14.6 mm at our phantom and 50.4 mm at the LDA phantom.

TABLES

Table 1
Various spin velocity distributions

Distribution	Statistical measure of dispersion	Expression
Gaussian	Standard deviation, σ	$\sigma = \sqrt{\dfrac{1}{k_{v_1}^2 - k_{v_2}^2}\, 2\ln\left(\left|S(k_{v_2})\right| / \left|S(k_{v_1})\right|\right)}$
Lorentzian	Half width at half maximum, Γ	$\Gamma = \pi\left(\left|k_{v_1}\right| - \left|k_{v_2}\right|\right)\ln\left(\left|S(k_{v_1})\right| / \left|S(k_{v_2})\right|\right)$
Boxcar[a]	Width of the box, W	$\dfrac{\left|S(k_{v_1})\right|}{\left|S(k_{v_2})\right|} = \dfrac{\left|k_{v_2}\right|\left|sin(k_{v_1}W/2)\right|}{\left(\left|k_{v_1}\right|\left|sin(k_{v_2}W/2)\right|\right)},\ -2\pi < W*k_v < 2\pi$

a) The expression containing W has to be solved numerically since it lacks a closed form solution. The boundaries of k_v arise from the requirement that $|S(k_v)|$ should be invertible.

Table 2
Imaging and flow parameters.

Parameter	Value		
Reynolds number [-]	500[a]	1000[a]	2000[a]
Mean flow velocity [m/s]	0.41[a]	0.82[a]	1.64[a]
VENC [cm/s]	30	120	170
Echo time [ms]	4.6	3.2	3.1

a) The Reynolds number and the mean flow velocity refer to the pre-stenotic part of the pipe. In the center of the stenosis, the Reynolds number is doubled and the mean flow velocity is increased four-fold.